Journal of Alloys and Compounds 636 (2015) 223–228

Contents lists available at ScienceDirect

Journal of Alloys and Compounds

journal homepage: www.elsevier.com/locate/jalcom

Solid state synthesis and characterization of Fe–ZrO_2 ferromagnetic nanocomposite thin films

V.G. Myagkov [a,*], L.E. Bykova [a], O.A. Bayukov [a], V.S. Zhigalov [a], I.A. Tambasov [a], S.M. Zharkov [a,b], A.A. Matsynin [a,b], G.N. Bondarenko [c]

[a] Kirensky Institute of Physics, Russian Academy of Sciences, Siberian Branch, Krasnoyarsk 660036, Russia
[b] Siberian Federal University, Krasnoyarsk 660041, Russia
[c] Institute of Chemistry and Chemical Technology, Russian Academy of Sciences, Siberian Branch, Krasnoyarsk 660049 Russia

ARTICLE INFO

Article history:
Received 13 October 2014
Received in revised form 19 January 2015
Accepted 2 February 2015
Available online 3 March 2015

Keywords:
Thermite reactions
Reactive films
Ferromagnetic nanocomposite films
ZrO_2

ABSTRACT

Fe–ZrO_2 ferromagnetic nanocomposite thin films are successfully synthesized using a thermite reaction between the Zr and Fe_2O_3 layers. The initial Zr/Fe_2O_3 bilayers were obtained by the deposition of Zr layers on α-Fe_2O_3 films at room temperature. The mixing at the Zr/Fe_2O_3 interface and synthesis of α-Fe and the amorphous ZrO_2 phases start at a temperature above the initiation temperature $T_{in} \sim 250$ °C. Together with the formation of α-Fe, partial transformation from Fe_2O_3 to Fe_3O_4 occurs after annealing at 300 °C. The secondary reaction between Fe_3O_4 and Zr starts soon after the Fe_2O_3 is converted to the Fe_3O_4 phase. The crystallization of amorphous ZrO_2 and the formation of the ZrO_2 cubic/tetragonal phase occurs above 400 °C. After annealing at 500 °C the reaction products contain (110) textured α-Fe nanocrystals with a diameter of about 34 nm embedded in an insulating c-ZrO_2 (or t-ZrO_2) matrix. The synthesized Fe–ZrO_2 nanocomposite films possess soft magnetic behavior, high magnetization and good chemical stability.

1. Introduction

Metal-ceramic nanocomposites have attracted a great deal of attention, both from the point of view of the fundamental perspective and for their potential applications due to high chemical inertness, refractory properties, high dielectric constant, wear resistance and high fracture toughness properties [1–3]. Zirconia ZrO_2 is one of the most important oxide ceramics. ZrO_2 has three stable polymorph modifications: the monoclinic (m-ZrO_2) from room-temperature up to 1170 °C, tetragonal (t-ZrO_2) between 1170 °C and 2370 °C, and cubic (c-ZrO_2) above 2370 °C. As is known, doping suitable metal cations is an effective way to stabilize the high temperature tetragonal t-ZrO_2 and cubic c-ZrO_2 phases at room temperature (RT). In particles the tetragonal t-ZrO_2 phase may also be stable in pure ZrO_2 [4–6]. Many physico-chemical properties of ZrO_2-based materials are determined by the relationship between these modifications, which strongly depend on the preparation conditions.

The fabrication of composites with nanoparticles of a transition metal (TM) embedded into a ZrO_2 matrix or TM doped ZrO_2 is challenging goal, however this can provide ZrO_2 with the magnetic properties that considerably enhance possibilities for applications. In recent years TM doped ZrO_2 thin films have received great attention, due to the theoretical predictions of room temperature magnetism in TM diluted oxides (DMO). Based on *ab initio* electronic structure calculations it was predicted that Mn doped c-ZrO_2 were to be ferromagnetic above 500 K [7]. However, the experimental results are ambiguous and show room temperature intrinsic ferromagnetism in Mn doped ZrO_2 above 400 K [8], defect-induced ferromagnetism [9] or the formation of non-magnetic phases [10]. The theoretical data also suggests the half-metallic properties and high temperature ferromagnetism of Fe doped ZrO_2 [7] or the formation of the antiferromagnetic ground state [11,12]. The experimental results show that doping ZrO_2 by Fe atoms stabilizes the formation of the tetragonal and cubic solid solutions, which are not magnetically ordered [13], antiferromagnetic [11] or have low magnetization [14,15] at room temperature. Contrary to solid solutions, magnetic Fe–ZrO_2 composites with nanoparticles of Fe and Fe_3O_4 embedded into the insulating ZrO_2 ceramic matrix prepared by the reduction in hydrogen of a totally stabilized $Zr_{0.9}Fe_{0.1}O_{1.95}$ solid solution [16], mechanical milling [17] and electron beam-physical vapor deposition, are to possess soft magnetic properties and relatively large saturation magnetization [18].

* Corresponding author.
E-mail address: miagkov@iph.krasn.ru (V.G. Myagkov).

http://dx.doi.org/10.1016/j.jallcom.2015.02.012
0925-8388/

In this work, we present a new approach to the formation of magnetic Fe–ZrO_2 nanocomposites using the thermite thin film reaction (1):

$$2Fe_2O_3 + 3Zr = 3ZrO_2 + 4Fe \quad \Delta H_r = 2790\ J/g \qquad (1)$$

Thermite mixtures belong to a wide class of energetic materials that contain a fuel (for example, Al, Mg, B, and Zr) and an oxidizer (WO_3, MoO_3, CuO, Bi_2O_3, and Fe_2O_3) [19]. These mixtures react with a release of large quantities of heat and may have a self-propagating high-temperature synthesis (SHS) mode. A typical combustion front, when the energetic mixtures contain micron-sized particles, has a propagation velocity on the order of several centimeters to a few meters per second and has a high front temperature above 3000 K [19–21]. In nanocomposite thermites (also termed nanostructured metastable intermolecular composites, nanothermites or superthermites), for which the size of the particles is reduced to the nanoscale, the combustion wave velocity reaches several km/s [22,23]. However, compared to other thermite reactions, thermochemical and material properties of reaction (1) for both nanothermites and traditional micron-sized thermites, is still imperfectly understood. Chigna et al. [24] prepared samples of Fe-doped c-ZrO_2 by thermite reaction (1) between powders of metallic Zr and α-Fe_2O_3 via combustion synthesis (SHS synthesis). Unexpectedly, under these synthesis conditions, the reaction products contained only a solid solution and did not contain pure α-Fe, according to reaction (1). Lv et al. [25] reported the combustion properties of α-Fe_2O_3/Zr composite particles and the highest combustion temperature reaching 2378 °C (2651 K), which is close to the calculated adiabatic temperature 2951 K [24]. The nanoporowders of Fe and ZrO_2 were synthesized from Fe_2O_3 and Zr by reaction (1) using high ball milling with average grain sizes of about 12 nm and 71 nm, respectively [26]. The study of nanothermites, containing a fuel and oxidizer in the nanofilm form, began in Al/CuO [27–30], Al/MoO_x [31] multilayers, Al/CuO bilayers [32], Fe_2O_3/Al nanothermite films [33] and Fe_2O_3/Al bilayers [34].

It is well known that solid-state reactions in thin films start at lower temperatures than in bulk materials. With the increase of the annealing temperature above the initiation temperature T_{in} at the interface, the formation of only one phase (first phase) occurs. Further increase of the annealing temperature leads to the formation of a phase sequence. At the moment there are no generally accepted theories predicting the first phase, phase sequence and the initiation temperature, although some models are available [35–38, and references therein]. However, in literature there are no reports about thermite reactions in Zr/Fe_2O_3 bilayers.

In this work, we demonstrate low-temperature thermite synthesis of Fe–ZrO_2 nanocomposite films containing ferromagnetic α-Fe nanoclusters separated by ZrO_2 grains. The final goal was to elucidate the sequence of the phases and structural transformations formed in the Zr/Fe_2O_3 bilayers after thermal annealing from 50 °C to 500 °C.

2. Experimental section

2.1. Synthesis

The initial films were obtained by the thermal deposition of Fe layers at a temperature of 250 °C onto NaCl(001) and chemically pure glass substrates having a thickness of 0.18 mm in vacuum at a residual pressure of 10^{-6} Torr. Previously, the substrates were degassed at 350 °C for 1 h. The α-Fe_2O_3 films were obtained by oxidation in an air environment of the intial Fe films at a temperature of 350 °C. The top Zr layer was deposited at room temperature to prevent a reaction between Zr and Fe_2O_3 during deposition. In these experiments, we used Zr/Fe_2O_3 bilayers with an approximate 4Fe:3Zr stoichiometry. The NaCl(001) films with thicknesses of Fe – 20 nm and Zr – 30 nm were prepared for transmission electron microscopy studies. In the rest of the experiments we used films on glass substrates with total thicknesses of 50–400 nm and only the experimental results for films with Fe thicknesses – 100 nm, Zr – 150 nm are presented here. The initial Zr/Fe_2O_3 bilayers were annealed at temperatures between 50 and 500 °C at 50 °C intervals. The samples were held at each temperature for 1 h. All synthesized Fe–ZrO_2 samples were obtained at a pressure of 10^{-6} Torr.

2.2. Characterization

The morphology and chemical composition of the films were investigated by transmission electron microscopy (TEM) using a JEOL JEM-2100, equipped with an energy-dispersive spectrometer (EDS) Oxford Inca x-sight, at the accelerating voltage of 200 kV. The phases formed during the synthesis process were identified using a DRON-4007 X-ray diffractometer (Cu Kα radiation). The thicknesses of the Zn and Fe_2O_3 layers were determined via X-ray fluorescent analysis. Mössbauer measurements were made with the conventional acceleration spectrometer MS-1104Em in transmission geometry with the source ^{57}Co in a Cr matrix at 296 K. The parameters of the hyperfine structure of the spectra were determined by fitting the model spectrum to an experimental spectrum in linear approximation by the least-squares method. The isomer shift value is relative to that of iron metal α-Fe at 293 K. The saturation magnetization M_S and in-plane hysteresis loops were measured by a vibrating sample magnetometer and were also controlled by torque measurements. For all samples the saturation magnetization M_S was determined relative to the initial α-Fe film value. The saturation magnetization M and the experimental determination of magnetic properties by a torque is described in detail in our previous work [39].

3. Results and discussion

The initial α-Fe films had saturation magnetization (M_0 = 217 emu/g) coinciding with the saturation magnetization of the bulk samples. Oxidation in air led to the formation of an α-Fe_2O_3 phase and sharp reduction of magnetization up to 2 emu/g. Since the magnetization of the α-Fe_2O_3 phase at room temperature is approximately 0.127 emu/g [40], one can make a conclusion that the oxidation products contain a small amount of magnetic oxides, such as γ-Fe_2O_3 and Fe_3O_4, in addition to the principal α-Fe_2O_3 phase. To avoid reactions between Zr and Fe_2O_3, the initial Zr/Fe_2O_3 bilayers were obtained from the deposition of a Zr layer on the Fe_2O_3 film at room temperature. The magnetization M_S of the initial Zr/Fe_2O_3 samples did not change after the deposition of the Zr layer.

The diffraction patterns of the initial Zr/Fe_2O_3 bilayers contained weak reflections from the fine-dispersed polycrystalline Zr and α-Fe_2O_3 phases (Fig. 1a). The RT Mössbauer spectra of the Zr/Fe_2O_3 bilayers for the initial sample and after annealing at 300 °C, 400 °C and 500 °C are presented in Fig. 2 and their

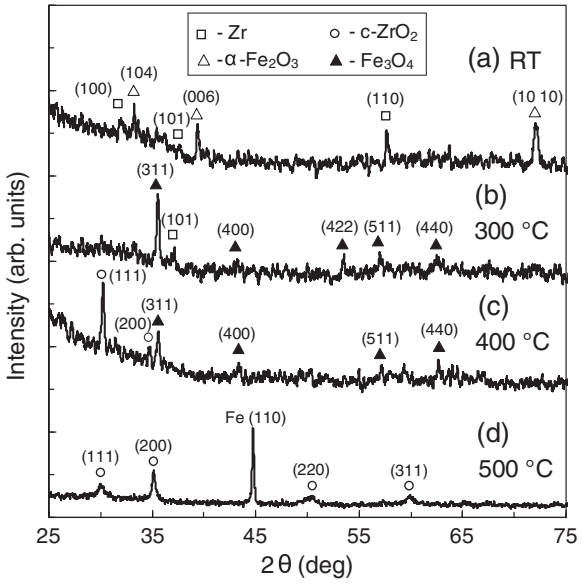

Fig. 1. (a) Typical XRD pattern of the initial Zr/Fe_2O_3 bilayers (a) and the synthesized Fe–ZrO_2 nanocomposites after annealing at 300 °C (b), 400 °C (c), 500 °C (d).

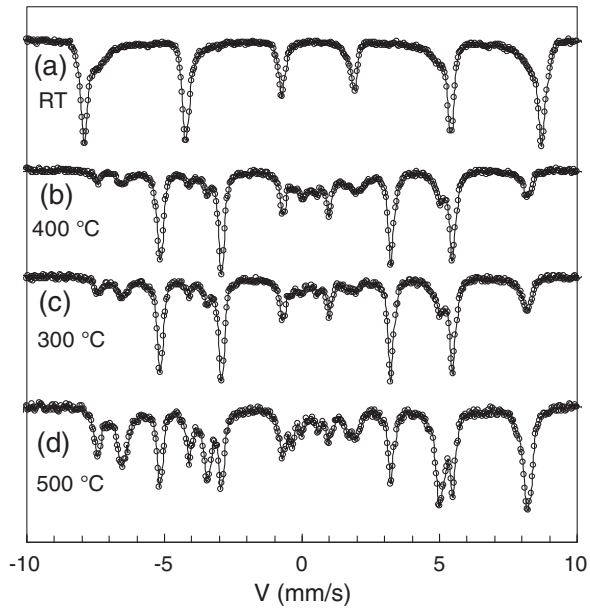

Fig. 2. Room temperature Mössbauer spectra of the initial Zr/Fe_2O_3 bilayers (a) and the synthesized $Fe–ZrO_2$ nanocomposite after annealing at 300 °C (b), 400 °C (c), 500 °C (d).

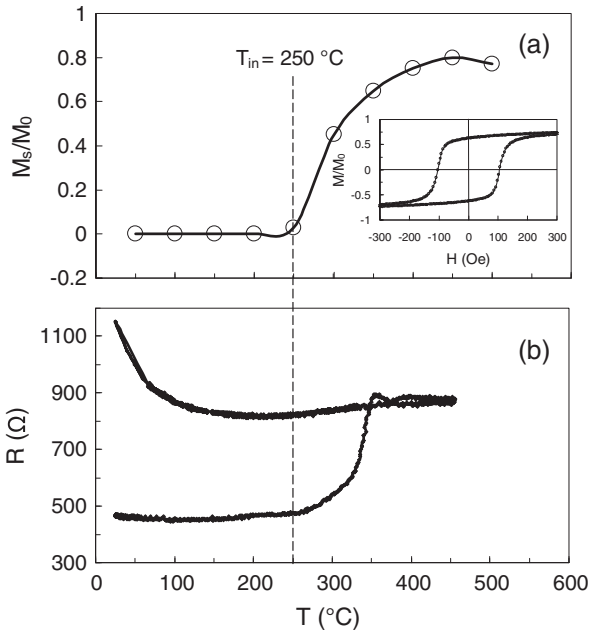

Fig. 3. (a) Relative magnetization M_S/M_0 as a function of annealing temperature for Zr/Fe_2O_3 bilayers. The inset shows the room temperature hysteresis loop of the synthesized $Zr–Fe_2O_3$ nanocomposite after annealing at 500 °C. (b) Electrical resistance of Zr/Fe_2O_3 bilayers heated to 500 °C at 2 °C/min as a function of temperature measurement.

parameter values are listed in Table 1. The Mössbauer data of the initial Zr/Fe_2O_3 bilayers show the formation of primary α-Fe_2O_3 (∼85%) and secondary γ-Fe_2O_3 (∼15%) phases (Table 1). The X-ray spectra did not contain reflections of the γ-Fe_2O_3 phase. However, the magnetic measurements account for the 5% content of the γ-Fe_2O_3 in the original sample. The obtained difference between the Mössbauer and magnetic data is due to the occurrence of an exchange interaction at the α-Fe_2O_3/γ-Fe_2O_3 interface, which leads to the antiferromagnetic ordering of the moments of the γ-Fe_2O_3 local areas. It gives the reduction of magnetization in the γ-Fe_2O_3 phase. These data provide clear evidence that the initial samples are Zr/Fe_2O_3 bilayers. Fig. 3 shows the relative magnetization M_S/M_0 and electrical resistance as a function of annealing temperature for the Zr/Fe_2O_3 bilayers. Up to 250 °C the saturation magnetization M_S in the initial Zr/Fe_2O_3 bilayers did not change, which indicates that there was no mixing or reaction between the Zr and Fe_2O_3 layers. With the increasing of the annealing temperature above 300 °C, the saturation magnetization M_S gradually increased and reached a maximum of $M_S \sim 0.8M_0$ close to 450 °C (Fig. 3a). From this it follows that reaction (1) has the initiation temperature $T_{in} \sim 250$ °C. A minor increase in the magnetization M_S occurs after annealing at 500 °C and indicates a start of the nonferromagnetic phase formation.

Fig. 3b shows the electrical resistance versus temperature for the Zr/Fe_2O_3 bilayers that are heated at 2 °C/min to 450 °C and cooled to room temperature. The temperature increase above T_{in} = 250 °C leads to a rapid increase in electrical resistance, which is undoubtedly due to the initiation and development of reaction (1). The electrical resistance above 400 °C does not depend on

Table 1
Mössbauer parameters for the Zr/Fe_2O_3 bilayers.

	IS, mm/s ±0.02	H, kOe ±3	QS, mm/s ±0.02	W, mm/s ±0.02	A ±0.03	Phase
(a) RT	0.383	516	−0.42	0.19	0.85	α-Fe_2O_3
	0.250	513	0	0.21	0.15	γ-Fe_2O_3
(b) 300 °C	0.28	488	−0.02	0.24	0.21	Fe_3O_4
	0.66	456	0.01	0.37	0.43	
	0.01	331	0	0.24	0.33	α-Fe
	0.16	–	0.57	0.22	0.03	Impurity phases
(c) 400 °C	0.27	487	−0.01	0.21	0.10	Fe_3O_4
	0.66	454	0.04	0.40	0.24	
	0.01	330	0.01	0.22	0.63	α-Fe
	0.13	–	0.53	0.23	0.03	Impurity phases
(d) 500 °C	0.28	488	0	0.21	0.07	Fe_3O_4
	0.67	455	−0.01	0.32	0.16	
	0.01	330	0	0.23	0.63	α-Fe
	0.14	–	0.52	0.23	0.03	Impurity phases
	1.02	–	1.89	0.85	0.11	FeO

Here IS is the isomer chemical shift relative to α-Fe, ±0.02 mm/s; H is the hyperfine magnetic field on Fe nuclei, ±5 kOe; QS is the quadrupole shift or splitting, ±0.03 mm/s; W is the linewidth of absorption, ±0.03 mm/s; S is the relative spectral area, ±0.05.

the annealing time and it follows that the reaction between Zr and Fe_2O_3 is fully completed.

After annealing at 300 °C the weak reflections from Fe_2O_3 disappear and a new peak (3 1 1) Fe_3O_4 is formed (Fig. 1b). The lack of α-Fe and ZrO_2 peaks implies that in the initial stage α-Fe becomes fine-crystalline and ZrO_2 is amorphous. The X-ray analysis is in close agreement with the Mössbauer data (Fig. 2b), which shows the formation of 64% Fe_3O_4 and 33% α-Fe in the reaction products (Table 1). It is suggested that in addition to the formation of α-Fe as provided by reaction (1), partial transformation of Fe_2O_3 to Fe_3O_4 occurs. Cao et al. [41] demonstrated that Fe_2O_3 nanoparticles were converted to crystalline Fe_3O_4 nanoparticles under vacuum or nitrogen atmosphere when heated to 420 °C.

Upon annealing the samples at 400 °C, the intensity of the (3 1 1) Fe_3O_4 peak decreases and a weak (1 1 0) α-Fe reflection begins to originate (Fig. 1c). This suggests the reduction of the content of the Fe_3O_4 fraction and expansion of α-Fe in the reaction product. The c-ZrO_2 and t-ZrO_2 phases have the proximity of the related peaks and thus these phases are unambiguously distinguished using only conventional X-ray diffraction. The formation of the (1 1 1) c-ZrO_2 (or t-ZrO_2) peak indicates the crystallization of amorphous ZrO_2 to a metastable c-ZrO_2 (or t-ZrO_2) phase. It is in good agreement with the Mössbauer data (Fig. 2c) which reveals the reduction of the content of Fe_3O_4 to 34% and the increase of α-Fe to 63% (Table 1). From this it is inferred that the accompanying reaction (2) between Fe_3O_4 and Zr starts soon after the Fe_2O_3 is converted to Fe_3O_4 phase:

$$2Zr + Fe_3O_4 = 3Fe + 2ZrO_2 \quad (2)$$

As the annealing temperature increases to 500 °C, in addition to the (1 1 1) peak other (2 0 0), (2 2 0), (3 1 1) peaks of c-ZrO_2/t-ZrO_2 phase can be observed (Fig. 1d) and no evidence of the m-ZrO_2 monoclinic phase appears. The formation of only the (1 1 0) α-Fe reflection shows that α-Fe nanoclusters are texturated along the substrate normal. According to the Scherrer equation, the average size of the α-Fe nanoclusters was estimated to be about 34 nm; and the size of c-ZrO_2/t-ZrO_2 grains calculated using the (1 1 1), (2 0 0), (2 2 0), (3 1 1) peaks was 110–140 nm. This indicates that the reaction products contain (1 1 0) texturated α-Fe grains which are separated by polycrystalline c-ZrO_2 (or t-ZrO_2) nanocrystals. The phase content of α-Fe (63%), determined from the Mössbauer spectra (Table 1) does not change and the Fe_3O_4 content decreases to 23% after annealing at 500 °C. The Mössbauer spectra contain one doublet with IS of ~1.02 mm/s, corresponding to the electronic configurations of Fe^{2+} in the octahedral site, characteristic of Fe^{2+} in FeO which is associated with the formation of wustite (FeO) [42]. The big value of the quadrupole splitting QS = 1.89 mm/s assumes that FeO form at the α-Fe grain boundary. This result can testify to partial (~11%) transformation of Fe_3O_4 to the paramagnetic FeO phase (Table 1) and it agrees well with the reduction of saturation magnetization (Fig. 3a) after annealing at 400 °C. After annealing at 300 °C, 400 °C and 500 °C the Mossbauer spectra contain a component (in Table 1 "impurity phases"), which is described as a doublet. Its small amount (~3%) hampers the estimate of the accurate Mossbauer parameters and phase identification. Hypothetically, this component can correspond to the FeC or FeN impurity phases, which are formed in the course of the reaction of Fe with carbon and nitrogen impurities. These impurities are believed to have arisen in the annealing chamber.

Fig. 4 shows a typical TEM image, selected area electron diffraction (SAED) pattern, high resolution transmission electron microscopy (HRTEM) image and EDS spectrum of the Fe–ZrO_2 film after annealing at 500 °C. The EDS analysis shows that the Fe–ZrO_2 films consist of Fe, Zr and O (Fig. 4d). The average atomic number for the ZrO_2 phase is lower than the atomic number of α-Fe thus the ZrO_2 region appears brighter on the TEM image (Fig. 4a) than

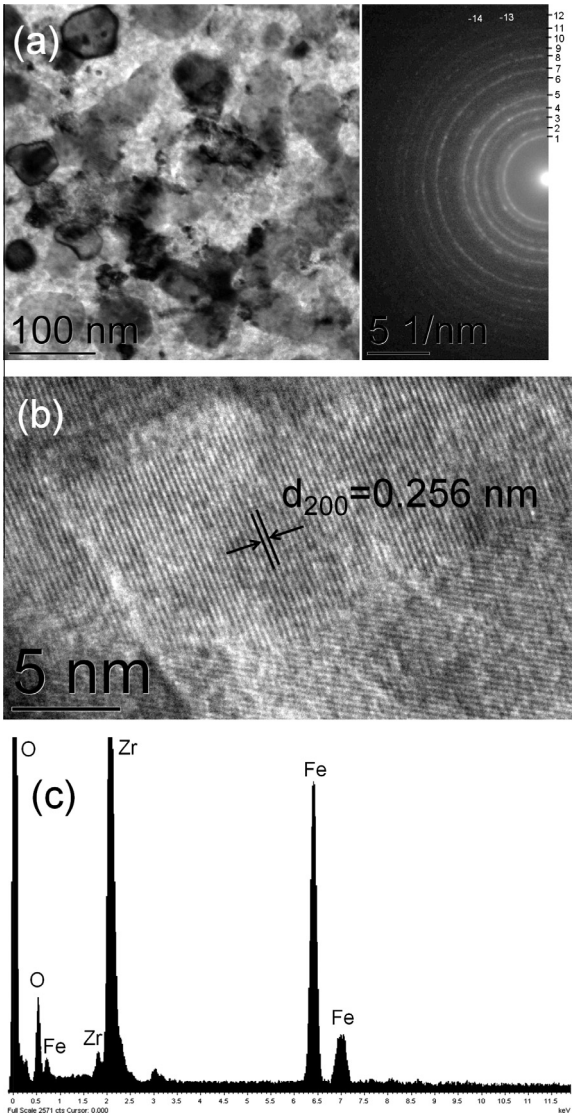

Fig. 4. TEM image (a), SAED pattern (b), HRTEM image (c), and, EDS spectrum (c) for the Fe–ZrO_2 film after annealing at 500 °C.

the α-Fe region. The dark regions correspond to the Fe grains and the light region – to the ZrO_2 matrix. The TEM observations (Fig. 4a) indicate that the α-Fe grains have a rough ring shape with a grain size of 10–60 nm and the α-Fe nanocrystallites have good uniformity in the reaction product. This grain size agrees with the average size of the α-Fe grains determined by XRD. The HRTEM image (Fig. 4c) of the Fe–ZrO_2 film after annealing at 500 °C shows lattice fringe spacing equal to 0.256 nm, which is in good agreement with the (2 0 0) atomic plane of c-ZrO_2/t-ZrO_2 phase. From this it follows that the ZrO_2 grains have (2 0 0)-preferred orientation and this finding is consistent with the XRD measurement. Although XRD could not distinguish tetragonal t-ZrO_2 from cubic c-ZrO_2 zirconia, the SAED pattern (Fig. 4c) interpretation confirms (see Table 2), that the c-ZrO_2 phase, rather than the t-ZrO_2, was stabilized during the thermite synthesis of the Fe–ZrO_2 composites.

The inset of Fig. 3a presents a typical in-plane hysteresis loop of a synthesized Fe–ZrO_2 film after annealing at 500 °C, which is characterized by a relative large value of the magnetic remanence (Mr) to M_S ratio (0.71). The large Mr/M_S value indicates that the Fe particles consist of randomly oriented equiaxial grains with cubic magnetocrystalline anisotropy [43]. The occurrence of hysteresis

Table 2
Indexing diffraction rings in Fig. 4b.

Rings	c-ZrO_2	t-ZrO_2	α-Fe	Fe_3O_4
1	(1 1 1)	(1 1 1)		(2 2 0)
2	(2 0 0)	(2 0 0)		(3 1 1)
3				(4 0 0)
4			(1 1 0)	
5	(2 2 0)	(2 0 2) (2 2 0)		
6	(3 1 1)	(1 1 3) (3 1 1)		
7	(2 2 2)	(2 2 2)		(4 4 0)
8				(5 1 1)
9			(2 0 0)	
10	(4 0 0)	(0 0 4) (4 0 0)		(5 3 3)
11	(3 3 1)	(3 1 3)	(2 1 1)	
12	(4 2 2)	(4 2 2)		(8 0 0)
13	(5 1 1)	(1 1 5)		(6 6 0)
14	(4 4 0)			

loops confirms that the size of the α-Fe nanoclusters in the Fe–ZrO_2 films is larger than the superparamagnetic critical size. According to the estimate in Ref. [44] the superparamagnetic critical size of transition metal nanoparticles ranges from 1 nm to 10 nm. Experimentally, the transition of Fe particles from ferromagnetic to superparamagnetic state is observed when the particle size is <24 nm [44,45].

Based on the Mössbauer data (Table 1) after annealing at 300 °C, 400 °C and 500 °C the volume fractions are equal to 33%, 63%, 63% for α-Fe; and to 64%, 34%, 23% for Fe_3O_4, respectively. We suppose, that the saturation magnetization of the synthesized α-Fe (1710 emu/cm^3) and Fe_3O_4 (477 emu/cm^3) phases are equal to the bulk sample values and estimate the relative values of magnetizations M_S/M_0 0.50, 072, 0.69 after annealing at 300 °C, 400 °C and 500 °C, respectively. The calculated values correspond closely to the experimental data presented in Fig. 3a. From this it follows that only α-Fe and Fe_3O_4 are the magnetic phases in the reaction products. The Mössbauer data do not indicate the presence of other iron oxides or phases of the Fe–Zr–O system.

Based on the above analysis the step-by-step evolution from Zr/Fe_2O_3 bilayers to Fe–ZrO_2 nanocomposite films was obtained, and the corresponding schematic illustration is presented in Fig. 5.

The extensive studies of the mechanism of a classical thermite reaction between Fe_2O_3 and Al (Goldschmidt reaction) by various groups indicates that the Fe_3O_4 formation and intermediate reactions, including the reaction between Fe_3O_4 and Al, occur before getting the final product [46–48]. It was well known that in

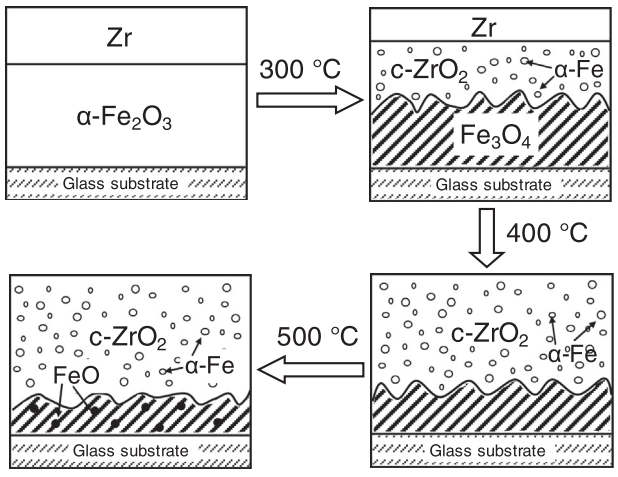

Fig. 5. Schematic illustration of solid-state synthesis of Fe–ZrO_2 nanocomposites by successive annealing of the Zr/Fe_2O_3 bilayers. Bright dots and dark dots denote α-Fe and FeO nanoclusters, respectively.

additions to the grain size, the important parameter of granular films is x_c, the percolation threshold. For the volume fraction $x > x_c$, nanograins can aggregate into a connecting network and initiate the metallic conductivity of the granular films. The initial Zr/Fe_2O_3 bilayer has the metallic conductivity determined by the Zr layer. After heating to 500 °C and sequential cooling to room temperature the electrical resistance of the synthesized Fe–ZrO_2 nanocomposite increases nearly four times relative to the initial Zr/Fe_2O_3 bilayer (Fig. 3b). However, the electrical resistance is about 10^{14} lower for pure ZrO_2 films with the same thickness at room temperature. From this it follows that the α-Fe nanograins have weak interconnection because they are separated by ZrO_2 interlayers and the volume fraction of the α-Fe nanograins is slightly below the percolation threshold. This result is in agreement with a rough estimate of the volume fraction of α-Fe $x \sim 0.5$ using Eqs. (1) and (2). This value is lower than the range limit $x_c = 0.5–0.6$ of the percolation threshold for many granular systems of metal nanoclusters embedded in dielectric matrix [49].

It is well known that thermite reactions in powders and free-standing multilayer foils are triggered by local heating and demonstrate the SHS mode at room temperature. Typically, thermite reactions in bilayers deposited on glass substrates occur in the SHS mode (combustion wave) above T_{in} and at heating rates >20 °C/s only [34,50]. However, at heating above $T_{in} = 250$ °C with rates >20 °C/s the thermite reaction in the Zr/Fe_2O_3 bilayers on glass substrates do not have the SHS regime. A possible explanation is in the fact that ZrO_2 has low thermal diffusivity ($0.63 \cdot 10^6$ m^2/c), which is about 20 times lower than that of Al_2O_3 ($13 \cdot 10^6$ m^2/c), which is a reaction product of Al-based thermite reactions. In the beginning, reaction (1) on the Zr/Fe_2O_3 interface of the ZrO_2 nanocrystals forms a heat-shielding interlayer which decreases heat exchange between the Zr and Fe_2O_3 films. This is a reason for the decreasing reaction rate and the SHS regime suppression.

After annealing at 500 °C the XRD patterns, magnetic and electrical properties do not change during 6 months, which suggests good temperature stability of the synthesized Fe–ZrO_2 samples. The heating rate and the choice of the subsequent annealing conditions are the controlling parameters which determine the formation of nanostructures, which, in turn, determine the physicochemical properties of the nanocomposite Fe–ZrO_2 thin films.

In summary, we demonstrated a new way to synthesize ferromagnetic Fe–ZrO_2 nanocomposite thin films. The initial Zr/Fe_2O_3 films were obtained by Fe film oxidation and sequential deposition of the Zr layer. Thermite reaction (1), using Zr and Fe_2O_3 films as a fuel and an oxidizer in Zr/Fe_2O_3 bilayers, starts above the initiation temperature $T_{in} = 250$ °C with the predominant formation of Fe, Fe_3O_4 and ZrO_2 phases. At annealing temperatures above 300 °C, the thermite reaction (2) between Fe_3O_4 and Zr starts. After 500 °C thermite reactions (1) and (2) reduce the magnetization of the Fe–ZrO_2 nanocomposite thin films to about 80% of the initial Zr/Fe_2O_3 film. The final products contain mainly the α-Fe nanograins separated by the c-ZrO_2 (or t-ZrO_2) matrix. The thermite method provides a promising route to the formation of Fe-ZrO_2 ferromagnetic nanocomposite thin films having low initiation temperature, soft magnetic properties, high magnetization and good chemical stability.

References

[1] H. Goesmann, C. Feldmann, Angew. Chem. Int. Ed. 49 (2010) 1362–1395.
[2] S. Bhaduri, S.B. Bhaduri, JOM 50 (1998) 44–51.
[3] S. Kubickova, J. Plocek, A. Mantlikova, J. Vejpravova, RSC Adv. 4 (2014) 5113–5121.
[4] N. Zink, F. Emmerling, T. Häger, M. Panthöfer, M.N. Tahir, U. Kolb, W. Tremel, Dalton Trans. 42 (2013) 432–440.
[5] R.C. Garvie, J. Phys. Chem. 69 (1965) 1238–1243.

[6] J.A. Navío, M.C. Hidalgo, G. Colón, S.G. Botta, M.I. Litter, Langmuir 17 (2001) 195–201.
[7] S. Ostanin, A. Ernst, L.M. Sandratskii, P. Bruno, M. Däne, I.D. Hughes, J.B. Staunton, W. Hergert, I. Mertig, J. Kudrnovský, Phys. Rev. Lett. 98 (2007) 016101-1–016101-4.
[8] N.H. Hong, C.-K. Park, A.T. Raghavender, O. Ciftja, N.S. Bingham, M.H. Phan, H. Srikanth, J. Appl. Phys. 111 (2012). pp. 07C302-1–07C302-3.
[9] J. Zippel, M. Lorenz, A. Setzer, G. Wagner, N. Sobolev, P. Esquinazi, M. Grundmann, J. Zippel, M. Lorenz, A. Setzer, G. Wagner, N. Sobolev, P. Esquinazi, M. Grundmann, Phys. Rev. B 82 (2010) 125209-1–125209-5.
[10] A. Pucci, G. Clavel, M.-G. Willinger, D. Zitoun, N. Pinna, J. Phys. Chem. C 113 (2009) 12048–12058.
[11] N.H. Hong, M.B. Kanoun, S. Goumri-Said, J.-H. Song, E. Chikoidze, Y. Dumont, A. Ruyter, M. Kurisu, J. Phys.: Condens. Matter 25 (2013) 436003-1–436003-7.
[12] A. Debernardi, D. Sangalli, A. Lamperti, E. Cianci, P. Lupo, F. Casoli, F. Albertini, L. Nasi, R. Ciprian, P. Torelli, J. Appl. Phys. 115 (2014). pp. 17D718-1–17D718-3.
[13] V.V. Kriventsov, D.I. Kochubey, Yu.V. Maximov, I.P. Suzdalev, M.V. Tsodikov, J.A. Navio, M.C. Hidalgo, G. Colón, Nucl. Instrum. Meth. A 470 (2001) 341–346.
[14] J. Okabayashi, S. Kono, Y. Yamada, K. Nomura, AIP Adv. 1 (2011) 042138-1–042138-7.
[15] D. Sangalli, E. Cianci, A. Lamperti, R. Ciprian, F. Albertini, F. Casoli, P. Lupo, L. Nasi, M. Campanini, A. Debernardi, Eur. Phys. J. B 86 (2013) 211-1–211-6.
[16] V.G. de Resende, F.L. Garcia, A. Peigney, E. De Grave, Ch. Laurent, J. Alloys Comp. 471 (2009) 204–210.
[17] S.C. Axtell, R. Schalek, J. Appl. Phys. 79 (1996) 5263–5265.
[18] X. Bi, J. Wang, W. Lan, S. Gong, H. Xu, J. Magn. Magn. Mater. 281 (2004) 290–294.
[19] E.L. Drezin, Prog. Energy Combust. Sci. 35 (2009) 141–167.
[20] L.L. Wang, Z.A. Munir, Y.M. Maximov, J. Mater. Sci. 28 (1993) 3693–3708.
[21] M.L. Pantoya, J.J. Granier, Propellants, Explos. Pyrot. 30 (2005) 53–62.
[22] J.A. Puszynski, J. Therm. Anal. Calorim. 96 (2009) 677–685.
[23] K.S. Martirosyan, L. Wang, A. Vicent, D. Luss, Nanotechnology 20 (2009) 405609-1–405609-8.
[24] P. Ghigna, G. Spinolo, U. Anselmi-Tamburini, F. Maglia, M. Dapiaggi, G. Spina, L. Cianchi, J. Am. Chem. Soc. 121 (1999) 301–307.
[25] B. Lv, Y. Xu, B. Hou, D. Wu, Y. Sun, Mater. Res. Bull. 43 (2008) 2769–2777.
[26] I.-J. Shon, H.-S. Kang, I.-Y. Ko, J.-K. Yoon, J.-M. Doh, Rev. Adv. Mater. 28 (2011) 1–4.
[27] Y. Yang, D. Xu, K. Zhang, J. Mater. Sci. 47 (2012) 1296–1305.
[28] P. Zhu, R. Shen, Y. Ye, Shuai Fu, D. Li, J. Appl. Phys. 113 (2013) 184505-1–184505-5.
[29] K.J. Blobaum, A.J. Wagner, J.M. Plitzko, D. Van Heerden, D.H. Fairbrother, T.P. Weihs, J. Appl. Phys. 94 (2003) 2923–2929.
[30] N.A. Manesh, S. Basu, R. Kumar, Combust. Flame 157 (2010) 476–480.
[31] S. Fu, Y. Zhu, D. Li, P. Zhu, B. Hu, Y. Ye, R. Shen, Eur. Phys. J. Appl. Phys. 64 (2013) 30301-1–30301-5.
[32] J. Kwon, J.M. Ducéré, P. Alphonse, M. Bahrami, M. Petrantoni, J.-F. Veyan, C. Tenailleau, A. Estève, C. Rossi, Y.J. Chabal, ACS Appl. Mater. Interfaces 5 (2013) 605–613.
[33] W. Zhang, B. Yin, R. Shen, J. Ye, J.A. Thomas, Y. Chao, ACS Appl. Mater. Interfaces 5 (2013) 239–242.
[34] V.G. Miagkov, K.P. Polyakova, G.N. Bondarenko, V.V. Polyakov, J. Magn. Magn. Mater. 258–259 (2003) 358–360.
[35] J.M. Poate, K.N. Tu, J.W. Mayer (Eds.), Thin Films-Interdiffusion and Reaction, Willey-Interscience, New York, 1978.
[36] E.G. Colgan, Mater. Sci. Rep. 5 (1990) 1–44.
[37] R. Pretorius, C.C. Theron, A. Vantomme, J.W. Mayer, Crit. Rev. Solid State Mater. Sci. 24 (1999) 1–62.
[38] T. Laurila, J. Molarius, Crit. Rev. Solid State Mater. Sci. 28 (2003) 185–230.
[39] V.G. Myagkov, V.S. Zhigalov, L.E. Bykova, G.N. Bondarenko, J. Magn. Magn. Mater. 305 (2006) 534–545.
[40] R. Skomski, J.M.D. Coey, Permanent Magnetism, Institute of Physics, Bristol, 1999.
[41] X. Cao, R. Prozorov, Yu. Koltypin, G. Kataby, I. Felner, A. Gedanken, J. Mater. Res. 12 (1997) 402–406.
[42] C.A. McCammon, D.C. Price, Phys. Chem. Miner. 11 (1985) 250–254.
[43] J.H. Fendle (Ed.), Nanoparticles and Nanostructured Films: Preparation, Characterization and Applications, WILEY_VCH Verlag GmbH & Co KGaA, NY, 1998.
[44] A.I. Gusev, A.A. Rempel, Nanocrystalline Materials, Cambridge International Science Publishing, 2004.
[45] P. Tartaj, C.J. Serna, J. Am. Chem. Soc. 125 (2003) 15754–15755.
[46] Y. Yang, D.-r. Yan, Y.-c. Dong, X.-g. Chen, L. Wang, Z.-h. Chu, J.-x. Zhang, J.-n. He, J. Alloys Comp. 579 (2013) 1–6.
[47] A. Babakhani, E. Zahabi, H.Y. Mehrabani, J. Alloys Comp. 514 (2012) 20–24.
[48] J.L. Chen, H.H. Hng, Y.W. Lee, S.W. Du, N.N. Thadhani, Combust. Flame 157 (2010) 2241–2249.
[49] C.L. Chien, J. Appl. Phys. 69 (1991) 5267–5272.
[50] V.G. Myagkov, I.A. Tambasov, O.A. Bayukov, V.S. Zhigalov, L.E. Bykova, Yu.L. Mikhlin, M.N. Volochaev, G.N. Bondarenko, J. Alloys Comp. 612 (2014) 189–194.